JACS
JOURNAL OF THE AMERICAN CHEMICAL SOCIETY
Article
pubs.acs.org/JACS

A Surfactant-Free Strategy for Synthesizing and Processing Intermetallic Platinum-Based Nanoparticle Catalysts

Hao Chen,[†] Deli Wang,[†] Yingchao Yu,[†] Kathryn A. Newton,[†] David A. Muller,[‡,§] Héctor Abruña,[†] and Francis J. DiSalvo*[,†]

[†]Department of Chemistry and Chemical Biology, Baker Laboratory, Cornell University, Ithaca, New York 14853-1301, United States
[‡]School of Applied and Engineering Physics, Cornell University, Ithaca, New York 14853, United States
[§]Kavli Institute, Cornell University, Ithaca, New York 14853, United States

Supporting Information

ABSTRACT: Using Pt_3Fe nanoparticles as an example, a surfactant-free Np-KCl matrix method (Np stands for nanoparticle) is developed for the synthesis of nanoparticles with controlled size and structure. In this method, the Np-KCl assembly is formed in a one-pot reduction in THF at room temperature. KCl is an insoluble byproduct of the reaction and serves as a matrix that traps the nanoparticles to avoid particle agglomeration and to control the coalescence of nanoparticles during thermal annealing up to 600 °C. By varying the molar ratio of metal precursors and KCl, as well as the time and temperature of annealing, the final particle sizes and crystalline order can be independently controlled. After thermal processing, nanoparticles were released from the KCl matrix and transferred in an ethylene glycol−water solution to support materials forming a uniform Np-support assembly. A detailed study of the synthesis of ordered intermetallic Pt_3Fe nanoparticles with an average diameter of 4 nm, using this Np-KCl method, is provided as an example of a generally applicable method. This surfactant-free strategy has been extended to the synthesis of other bi- and trimetallic nanoparticles of Pt-transition metals.

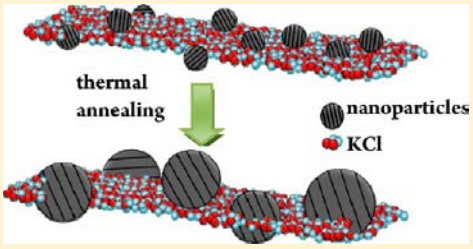

INTRODUCTION

Nanoparticles with controlled size and composition are of great interest for different applications, such as in optical and electronic devices,[1,2] or in electronic[3] and magnetic memories.[4,5] Because of their tailored electronic structure and surface chemistry, bimetallic Pt alloy nanoparticles have long been used as catalyst materials, especially for energy applications such as fuel cells,[6−10] electrolytic water splitting,[11] and lithium ion batteries.[12−14] Owing to their unique electronic structure, Pt_3M (M = transition metal) alloy nanoparticles, especially, Pt_3Fe, Pt_3Co, and Pt_3Ni, have been extensively explored as catalysts for the oxygen reduction reaction (ORR) in polymer electrolyte membrane fuel cells (PEMFCs).[6,7]

For several decades the synthesis of Pt-based bimetallic nanoparticles has relied on using different long-chain surfactant molecules. These surfactants are used to control nanoparticle size as well as to prevent particle aggregation. There are still two fundamental issues in terms of the use of surfactants: (1) surfactants may block surface reaction sites, limiting their catalytic activity; (2) thermal annealing of the nanoparticles is often needed to develop atomic order or promote growth of certain facets. Under the latter conditions the surfactant may decompose, leaving surface residues that deactivate the catalyst; even if clean surfaces are obtained, aggregation of the nanoparticles leads to significant decreases in active surface area per mass of catalyst. Some groups have reported the use of MgO[5,15] or SiO_2 coatings[16−18] to prevent aggregation, in which surfactants were still involved in key steps during the synthesis. Some solution-phase chemical synthesis methods do form nanoparticles on support materials without using any surfactant;[19] however, such methods do not usually permit independent control of particle size, phase, or composition, as well as nanoparticle loading.

Another approach to achieve clean surfaces is based on using ethylene glycol as both the reducing agent and protecting ligand, which provides simultaneous control over particle size and composition.[20,21] In this case, ethylene glycol was decomposed electrochemically at high potentials or by heat treatment below 175 °C, leaving relatively clean surfaces. Generally, this process is suitable for producing nanoparticles of the more electronegative elements, such as Au, Pt, Rh, Ru.[22,23] Alloys and intermetallic phases are difficult to prepare, since the reduction rates for different elements vary widely. In any case, ethylene glycol that binds to the metal surface is thought to be oxidized or decomposed under heat treatment, especially above 150 °C, which makes it very challenging to anneal at higher temperatures to increase particle size or to obtain an ordered intermetallic phase without significant particle agglomeration.[20]

The ordered intermetallic phases of Pt-M (M = transition metal) nanoparticles, when compared to their disordered alloy phases, have been demonstrated to be better catalysts for fuel

Received: August 31, 2012
Published: October 11, 2012

   dx.doi.org/10.1021/ja308674b | J. Am. Chem. Soc. 2012, 134, 18453−18459

cell applications owing to their enhanced stability and poison tolerance.[9,24−27] To provide a large surface area, the synthesis targets small particle sizes. However, when the nanoparticle sizes are too small (smaller than 3 nm in the case of pure Pt), these particles go through dissolution and coarsening, rendering poor stability.[28] A comprehensive theoretical study showed that, in the cathode environment of PEMFCs, the particle morphology and size of Pt nanoparticles larger than 4 nm are relatively stable.[29] However, a key challenge has remained for the current surfactant-free synthetic methodologies to achieve such small particle sizes during the inevitable thermal annealing process to form the preferred ordered intermetallic structure.[30]

Here we report a new and surfactant-free approach for the preparation and handling of nanoparticles with controlled size and phase by using an ionic salt as a protective matrix during thermal annealing to limit nanoparticle growth. Using the preparation of ordered intermetallic Pt_3Fe nanoparticles as an example, the synthesis and stabilization strategy is shown in Figure 1. The Pt−Fe nanoparticles were formed and protected

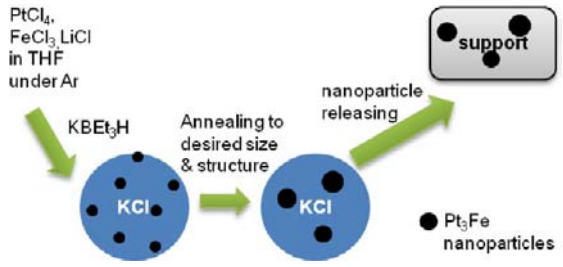

Figure 1. Scheme for the synthesis and transfer of Pt_3Fe nanoparticles to support materials by using the Np-KCl matrix method. Pt_3Fe nanoparticles are formed in a quick room temperature reduction of a THF solution of metal chlorides using KEt_3BH as the reducing agent. Since the byproduct KCl is not soluble in THF, the newly formed Pt_3Fe nanoparticles are trapped in the solid KCl. During thermal annealing, nanoparticles very slowly grow in the KCl matrix to form somewhat larger particles, while the Pt and Fe atoms order to form an intermetallic compound. After annealing, Pt_3Fe nanoparticles can be transferred to appropriate supports by dissolving the KCl salt in ethylene glycol.

by an insoluble byproduct, in this case KCl, in a THF solution. Instead of separate synthesis and protection steps, the Np-KCl matrix was formed by a rapid room temperature liquid phase reduction of mixed-metal chloride salts in THF. The KCl matrix protects the nanoparticles from aggregating during the synthesis and subsequent thermal annealing up to 600 °C. The nanoparticles can then be released from the KCl and uniformly bound to a catalyst support in a mixed solvent of ethylene glycol and water under sonication.

Under the conditions reported here, the nanoparticles made at room temperature in the KCl matrix are around 2 nm in diameter. They then serve as "building blocks" and diffuse in or on the KCl matrix to form larger particles. By controlling the annealing temperature/time and the molar ratio of metals to KCl salt, final particle sizes and phases can be controlled at the same time. To demonstrate the generality of this method, bi- and trimetallic Pt−M (M = transition metal) intermetallic phases with different structure types and electronegativities of M were prepared by this technique, including Pt_3Mn, PtNi and Pt_2CoFe. This paper focuses on the preparation of Pt_3Fe to illustrate the details of the method and the range of parameters that determinine particle structures, morphologies, etc.

EXPERIMENTAL SECTION

Synthesis. All the chemicals were purchased from STREM Chemicals Inc. or are otherwise listed individually. Pt_3Fe-15KCl was synthesized as follows: 0.12 mmol $PtCl_4$ and 0.04 mmol $FeCl_3$ were weighed out in an argon-filled glovebox and dissolved in 10 mL of THF by stirring. The reducing agent KEt_3BH (1.0 M in THF, Sigma-Aldrich) with 30 mol % excess was mixed with THF to form a 15 mL solution. Then the precursor solution was drawn up into a syringe and injected into a solution of the reducing agent under vigorous stirring. The mixing immediately (within seconds) formed an opaque black suspension as previously observed.[30] The sample was dried under vacuum until most of the THF was gone. Hexanes were then added to precipitate the Np-KCl powders. The sample was then washed three times with THF and hexanes without contacting air. The product was then dried under vacuum for 2 h and transferred to the glovebox. The product was placed into silica tubes, which were sealed under vacuum and then annealed at different temperatures. To synthesize Pt_3Fe-40KCl and Pt_3Fe-80KCl, LiCl was added into the precursor solution to obtain a higher ratio of Cl^- to metal. An equivalent amount of KEt_3BH was added to precipitate all the Cl^- as KCl, as described in eq 2.

Electrochemical Measurements. Electrochemical experiments were conducted in 0.1 M $HClO_4$ at room temperature with a rotating disk electrode using a Solartron electrochemistry station. A reversible hydrogen electrode (RHE) and a Pt wire were used as reference and counter electrodes, respectively. Catalysts inks were prepared by mixing the catalysts with Nafion (0.05 wt % Nafion dissolved in ethanol). The ink solutions were deposited on glassy carbon electrodes and dried in air to serve as the working electrode. For the specific activity evaluation, the electrochemical surface areas (ECSA) of Pt were calculated by integrating the average areas of hydrogen adsorption and desorption, using a conversion factor of 200 $\mu C\ cm^{-2}$. The ORR polarization curves were obtained by sweeping the potential from +0.1 to +1.1 V anodically at a scan rate of 5 mV s^{-1} and rotation rate of 1600 rpm. The specific activities for mass and surface area were established at 0.85 and 0.90 V based on ORR polarization curves using the Koutecky−Levich equation, which can be described as:

$$\frac{1}{I} = \frac{1}{I_d} + \frac{1}{I_k}$$

where I is the overall current density, which is the experimentally measured current; I_d is the diffusion-limited current density, which we choose as the current at 0.4 V measured from the ORR polarization curves, and I_k is the kinetic current density at the potential of interest. All electrochemical measurements were conducted at 21 °C.

Materials Characterization. The synthesized Pt_3Fe nanoparticles were characterized by powder X-ray diffraction using a Rigaku Ultima VI diffractometer, and diffraction patterns were collected at a scanning rate of 5 °/min at steps of 0.02 °. Low resolution TEM was performed using a Tecnai T12 operated at 120 kV. High resolution STEM/EDX images were obtained from a Shottky-field-emission-gun Tecnai F20 operated at 200 kV with an installed monochromator. The STEM/EELS data were acquired on a fifth-order aberration-corrected scanning transmission electron microscope (Nion UltraSTEM) operated at 60 kV, with convergence angle α_{max} = ~30 mrad.

RESULTS AND DISCUSSION

Np-KCl Matrix. The formation of Pt_3Fe nanoparticles and KCl salt in a THF solution is given in the following equation:

$$3PtCl_4 + FeCl_3 + 15KEt_3BH \rightarrow Pt_3Fe + 15KCl + 7.5H_2 + 15Et_3B \quad (1)$$

Pt_3Fe nanoparticles were formed in a very rapid solution-based reduction of their chloride precursors by using KEt_3BH as the reducing agent and THF as the solvent. Apart from the nanoparticles, only one of the byproducts, KCl, is not soluble in

dx.doi.org/10.1021/ja308674b | J. Am. Chem. Soc. 2012, 134, 18453−18459

THF.[31] Therefore, after reduction, both of these products precipitate. For the synthesis of Pt_3Fe-15KCl (eq 1), after injection of KEt_3BH, a black precipitate was quickly formed, leaving a clear supernatant. After decanting the supernatant, rinsing with THF, and vacuum drying, the precipitates were taken to the TEM. As shown in Figure 2a, the black dots are

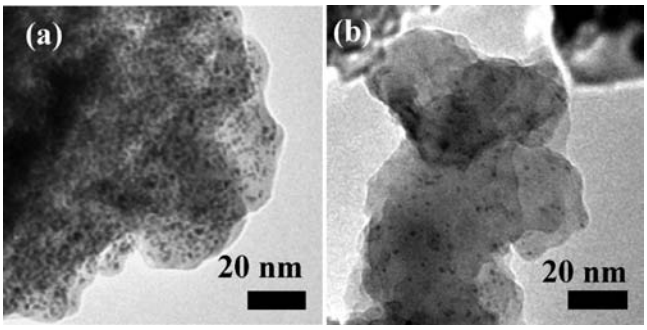

Figure 2. (a) TEM image of the Pt_3Fe-15KCl product obtained by room temperature reduction. (b) TEM image of Pt_3Fe-160KCl synthesized at room temperature. The small dark spots are the alloyed Pt−Fe nanoparticles.

the Pt−Fe nanoparticles, and the gray area is the KCl. The average diameter for the Pt_3Fe nanoparticles was approximately 1.8 ± 0.2 nm (Figure S1 in Supporting Information [SI]).

Since both LiCl and KEt_3BH are dissociated into ions in THF (LiCl has a solubility of 4.6 wt % in THF[32]), as shown in eq 2, the molar ratio of Pt_3Fe to KCl can be altered by adding LiCl to the metal chloride salt solution and also adding excess reducing agent as follows:

$$3PtCl_4 + FeCl_3 + xLiCl + (15 + x)KEt_3BH \rightarrow Pt_3Fe + (15 + x)KCl + 7.5H_2 + 15Et_3B + xLiEt_3BH \quad (2)$$

Np-KCl assemblies are formed at room temperature, independent of x (at least up to x = 145). Pt_3Fe-40KCl, Pt_3Fe-80KCl, and Pt_3Fe-160KCl were made with x = 25, 65, and 145 respectively. The TEM image of the as-made sample of Pt_3Fe-160KCl is shown in Figure 2b. As the amount of KCl increases, the Pt_3Fe nanoparticles are still well dispersed but "diluted" in the KCl matrix. The distance between Pt_3Fe nanoparticles in Pt_3Fe-160KCl increases compared to that of the Pt_3Fe-15KCl.

The X-ray diffraction pattern of the as-synthesized Pt−Fe product obtained at room temperature, both before and after washing with water (in the presence or absence of KCl), (Figure S2 in SI) shows roughly 2-nm diameter domain sizes, which agrees with particle sizes observed in the TEM images. As expected, the average composition of an ensemble of nanoparticles in an area of 500 nm by 500 nm obtained by energy-dispersive X-ray (EDX) spectroscopy for Pt/Fe was typically 75:25 (±3%) and uniform throughout the sample (Figure S3 in SI). In order to obtain larger particles and to develop an ordered crystal structure, the product must be annealed without particle sintering.

Synthesis of 4-nm Ordered Pt_3Fe Nanoparticles. Ordered intermetallic Pt_3Fe nanoparticles were obtained without significant growth in particle size by thermal annealing of the dried as-made nanoparticle−salt matrix samples of Pt_3Fe-15KCl, Pt_3Fe-40KCl, Pt_3Fe-80KCl, and Pt_3Fe-160KCl at 600 °C for 12 h.

For samples with the highest KCl content, the size of Pt_3Fe nanoparticles increased by only factors of ∼2 upon thermal annealing. In comparison, when no extra salt was present, the domain size, as determined by X-ray diffraction, increased by a factor of 4−5, and significant interparticle sintering occurred. Ostwald-like ripening and particle coalescence are the likely mechanisms for nanoparticle growth.

Not surprisingly, we observe that the annealing temperature and the molar ratio of Np to salt play an important role in the particle sizes. The TEM images of Pt_3Fe-40KCl annealed at 400, 500, and 600 °C for 12 h are shown respectively in a−c of Figure 3. As the annealing temperature increases, the particle sizes increase.

To explore the effects of changing the molar ratio of Pt_3Fe to KCl, the annealed samples were sonicated in a solution of ethylene glycol and water to remove the salt. Since the Pt_3Fe nanoparticles can be temporarily stabilized by the "dielectric" properties of ethylene glycol,[21] a small drop of the suspended particles were quickly transferred to the TEM grid. The TEM

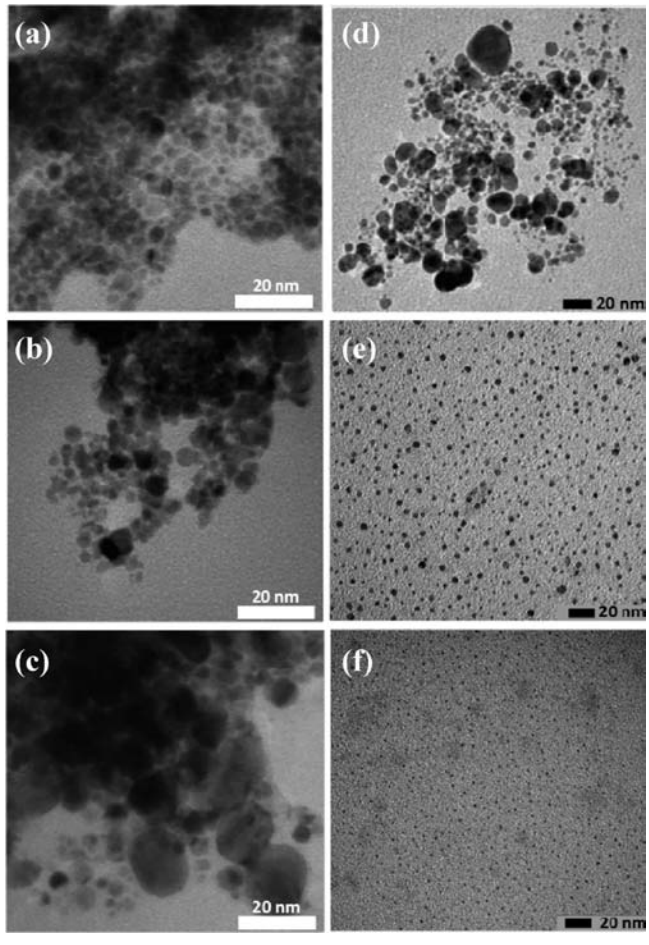

Figure 3. TEM images of Pt_3Fe-40KCl annealed at (a) 400 °C, (b) 500 °C, and (c) 600 °C for 12 h. The rate of growth of the nanoparticles in the KCl matrix increases as the annealing temperature increases, resulting in larger particle sizes. TEM images of (d) Pt_3Fe-15KCl, (e) Pt_3Fe-80KCl, and (f) Pt_3Fe-160KCl, annealed at 600 °C for 12 h. By increasing the molar ratio of salt to nanoparticle precursors, the growth of nanoparticles in the KCl matrix is better controlled.

dx.doi.org/10.1021/ja308674b | J. Am. Chem. Soc. 2012, 134, 18453−18459

image of the desalted Pt_3Fe-15KCl-600 °C 12-h sample is shown in Figure 3d. Particle sizes vary from 2 nm to larger than 20 nm. There was essentially no size control in this case. On the other hand, the TEM image of the desalted Pt_3Fe-80KCl-600 °C 12-h sample showed a much narrower particle size distribution (Figure 3e). The majority of particle diameters are between 3 and 6 nm, with an average particle size of 4 nm based on statistics from determining the diameters of more than 200 particles (Figure S4 in SI). Similarly, as shown in Figure 3f, further increasing the molar ratio of KCl/Pt_3Fe to 160:1 results in even smaller particle sizes after thermal annealing. An average particle size of ~2.5 nm is obtained on the basis of statistics from more than 250 particles from Pt_3Fe-160KCl annealed at 600 °C for 12 h (Figure S5 in SI). Notice that in a and b of Figure 2, the Pt_3Fe nanoparticles are similar in size for the as-made (room temperature) samples, but after thermal annealing at 600 °C for 12 h, the one with the least salt loses size control.

With a higher molar ratio of metal precursors to KCl, the nanoparticles are very close to each other. At 600 °C, which is close to the melting temperature of KCl (771 °C), the diffusion rate is apparently high enough to produce significant particle growth. However, with a lower particle density in the KCl matrix, the particles are efficiently separated so that particle growth is much slower.

The X-ray diffraction (XRD) patterns of the four annealed samples are shown in Figure 4. The only peaks observed are

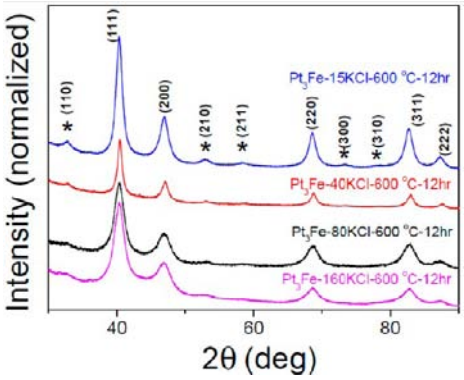

Figure 4. XRD patterns of all four samples of Pt_3Fe-15KCl(blue), Pt_3Fe-40KCl(red), Pt_3Fe-80KCl(black), and Pt_3Fe-160KCl(purple) annealed at 600 °C for 12 h, show the Pt_3Fe intermetallic phase. The peak positions for the ordered intermetallic phase of Pt_3Fe are marked with *. These weak ordered superlattice peaks are visible in all four samples.

indexed by the ordered cubic structure of Pt_3Fe. No peaks corresponding to Pt, Fe, other intermetallics in the Pt−Fe phase diagram (such as the 1:1 PtFe intermetallic phase), or any other Pt- or Fe-containing compounds are present in the diffraction pattern. The observation of ordering peaks, such as the expected weak (110), (210), and (211) peaks, demonstrates that the desired ordered intermetallic phase rather than the disordered alloy phase of Pt−Fe was prepared for all four samples. On the basis of the Scherrer equation, average crystal domain sizes of 4 and 3.4 nm are calculated from the line widths of the XRD patterns for Pt_3Fe-80KCl-600 °C-12 h and Pt_3Fe-160KCl-600 °C-12 h, respectively.

The particle sizes calculated from TEM images of Pt_3Fe-160KC-600 °C-12 h are only slightly smaller than the value calculated from XRD, indicating that each particle is a single crystal. The small difference may due to the volume-weighted nature of XRD measurements, which tend to overestimate the geometric particle size.[33] To better study these small ordered intermetallic nanoparticles, we have also evaluated the atomic level distribution of Pt and Fe in Pt_3Fe-160KCl annealed at 600 °C by performing annular dark-field STEM (ADF-STEM) and electron-energy loss spectroscopy (EELS) imaging. The sample was washed with water to remove KCl and then transferred to a TEM grid for TEM and EELS studies. An ADF-STEM overview image of a representative region is shown in Figure 5a. In Figure 5b, a 2.5 nm Pt_3Fe nanoparticle is viewed along

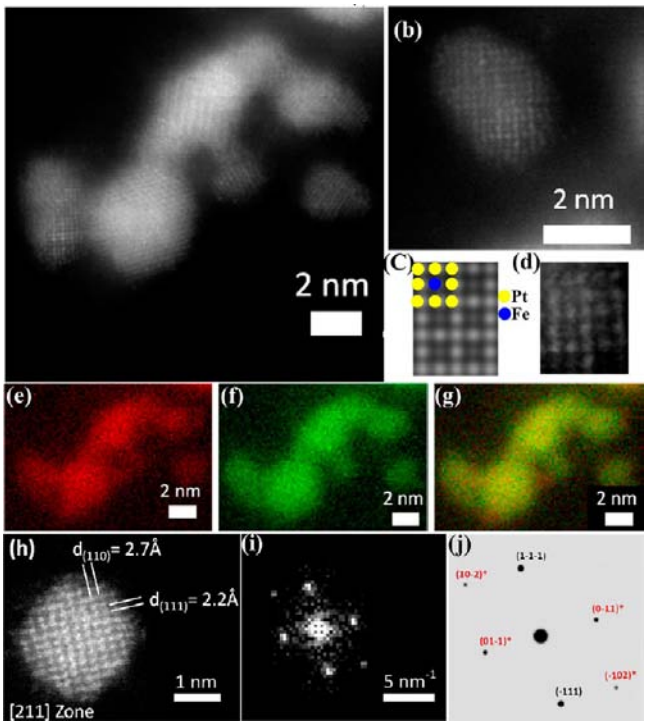

Figure 5. (a) Annular dark-field STEM (ADF-STEM) overview image of the thermally annealed ordered Pt_3Fe nanoparticles. (b) An ADF-STEM image of an ordered Pt_3Fe particle projected along the [100] axis. (c) A model ADF-STEM image of the projection of an ordered Pt_3Fe particle along the [100] axis. (d) An expanded view of a section of the super lattice features from (b). The 2-D EELS maps of (a) are shown in, (e) for Fe and (f) for Pt along with the (g) composite Fe vs Pt map. (h) HAADF-STEM image of one Pt_3Fe nanoparticle on [211] zone axis, with (i) diffraction pattern showing the intermetallic superlattice peaks of {110} and {210}. (j) Simulated diffraction pattern (contrast inverted) from [211] zone axis, which matches the experimental diffraction pattern in (i). The intermetallic peaks are in red and marked by *.

the [100] zone axis. Due to the unique super periods that are not present in the disordered alloy phase, the $L1_2$ ordered intermetallic structure in Pt_3Fe can be directly identified. For example, for the ordered intermetallic particles, along the [100] axis, the projected unit cell is composed of a periodic square array of pure Fe columns surrounded by Pt columns at the edges and corners of each unit cell (Figure 5c). Because of the 'Z-contrast' of Pt and Fe, the Pt columns will have an intensity higher than that of the Fe columns in ADF-STEM images (Figure 5a,b).[34,35] This differs from the disordered alloy phase, which has all columns with random distribution of atoms. A demonstration of such ordered structure along the [100] axis is shown in Figure 5c. A cropped area of an experimental ADF-

dx.doi.org/10.1021/ja308674b | J. Am. Chem. Soc. 2012, 134, 18453−18459

STEM image of the particle in Figure 5b shows a similar pattern (Figure 5d). This ordered intermetallic structure can also be observed along other zone axes. In Figure 5h, an ordered nanoparticle with a 2.5 nm diameter is viewed along the [211] zone axis. The lattice spacings of 2.7 Å and 2.2 Å are attributed to (110) and (111) lattice fringes; both values are matched with the bulk Pt_3Fe intermetallic structure. The fast Fourier transform (FFT) pattern of this nanoparticle is shown in Figure 5i; the diffraction spots from the {110} and {210} superlattice reflections clearly show that the ordered structure was achieved. To further confirm the ordering, we have simulated the diffraction patterns of an ideal Pt_3Fe fcc crystal along its [211] zone axis, and the simulated result in Figure 5j matches the experimental result in Figure 5i. This is conclusive evidence that the intermetallic structure is stable even as ultrasmall size (~3 nm) nanoparticles after thermal annealing. On the basis of the ADF-STEM images along with the appearance of superlattice peaks in XRD (Figure 4), we confirm that at least a majority of the annealed particles are atomically ordered. The EELS maps of Fe, Pt, and their composite are shown in e–g of Figure 5, respectively. The signals from Fe are extracted by using a power-law background fit of the Fe-$L_{2,3}$ edge, since the peaks have distinct and abrupt onsets. However, due to the delayed onset and breadth of the Pt–M and Pt–N edges, we have used a MCR (multivariate component resolution) method to extract a Pt–N_3 edge. The reliability of this method for the Pt–N_3 edge has been verified in our previous publications.[36] From the EELS images, a homogeneous distribution of Fe and Pt is observed, with no obvious phase segregation (Figure 5e–g).

Transfer to Support Materials. In order to use the annealed nanoparticles as fuel cell catalysts, they were released from the KCl matrix and bound to a conducting carbon black support (Vulcan X-72). This was accomplished by dissolving the KCl and protecting the Pt_3Fe in a solution of ethylene glycol (ethylene glycol and water with a volume ratio of 27 to 1) that contained the carbon support as a well-dispersed suspension (Figure 6b). Since the ethylene glycol can temporarily stabilize the Pt-based nanoparticles,[20,21] the nanoparticles were transferred to the carbon support without significant agglomeration and with good dispersion (Figure 6b,d). In contrast, significant agglomeration is observed when a mixture of isopropanol and water (27:1 by volume) (Figure 6c) or pure water (Figure 6a) was used as the solvent to transfer these nanoparticles. Temperature-programmed desorption (TPD) studies and density functional theory (DFT) calculations[37–40] showed that, on different Pt-based mono- or bimetallic surfaces, the ethylene glycol completely decomposes under vacuum, to H_2, CO, or CO_2 up to 175 °C. At such temperatures, obvious nanoparticle sintering does not occur on carbon black,[41] and a relatively clean surface is obtained. Ten weight percent Pt_3Fe-80KCl-600 °C-12 h supported by Vulcan carbon has been prepared and processed using the above transfer method. A TEM image of the product (Pt_3Fe/C) is shown in Figure 6d. Little aggregation of the nanoparticles or changes in particle sizes was observed. To be sure that most of the nanoparticles are bound to the carbon, the loading of the Pt_3Fe was independently determined by thermogravimetric analysis (TGA) of the product by heating in air to remove the carbon as CO_2 and oxidizing the Fe to Fe_2O_3. The TGA data showed a Pt_3Fe loading of 10 wt % (Figure S6 in SI). The detailed electrochemistry study on the ORR activities is shown in Figure S7 in SI. Here, we used this Pt_3Fe system as an example to demonstrate the synthesis and handling of intermetallic nanoparticles using the Np-KCl method. This method provided a general way to synthesize the electrochemically interested nanoparticles, such as Pt–Cu,[42–45] Pt–Co,[46–48] and Pt–Ni.[49–52]

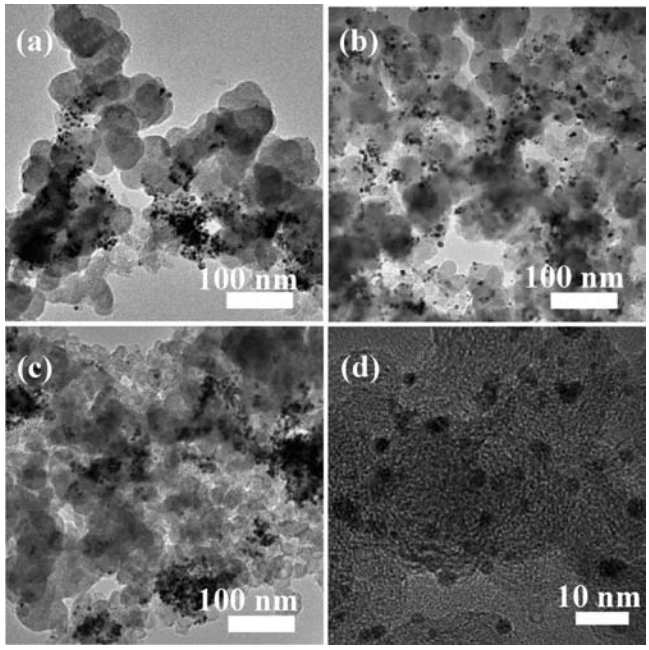

Figure 6. TEM images of 10 wt % Pt_3Fe-80KCl-600 °C-12 h supported by carbon black (Pt_3Fe/C). Pt_3Fe-80KCl-600 °C-12 h and carbon black were weighed out and placed in the scintillation vial. Three milliliters of solvent was then added into the vial. The mixtures were then ultrasonicated (Microson ultrasonic cell disruptor) for 10 min at power level 4. After sonication, the mixture was then stirred for 24 h. (a) Just water as solvent; (b) ethylene glycol and water with a volume ratio of 27:1 as solvent; (c) isopropanol and water with a volume ratio of 27:1 as solvent; (d) an enlarged image of a typical area in (b). In (b) and (d), after stirring for 24 h, the powder was subsequently washed by water to remove any remaining KCl and heated to 175 °C for half an hour to remove any ethylene glycol absorbed on the particle surface.

Synthesis of Other Pt–M Ordered Nanoparticles. We have extended this synthesis method to other Pt-based nanoparticle systems. A wide variety of chloride metal salts are soluble in THF, either as binary chlorides or as ternary lithium metal chloride salts. Upon reduction with $KBEt_3H$, the resultant metal nanoparticles are trapped in KCl. To achieve ordering and homogeneity, the Np-KCl product is again annealed at temperatures up to 600 °C. Mn has an electronegativity of 1.5, which makes it more difficult to reduce than Fe (electronegativity of 1.8). Using the method provided here, the ordered intermetallic form of Pt_3Mn has been synthesized. Similarly, bi- and trimetallic nanoparticles of PtNi and Pt_2CoFe with a tetragonal ordered intermetallic structure were also synthesized and transferred to vulcan carbon support using this method (Figure S8 in SI). The average compositions of an ensemble of nanoparticles in an area of 500 nm by 500 nm for all three samples were examed by EDX spectroscopy and showed the desired stoichiometic ratios (Figure S9 in SI). The normalized signal of scanning transmission electron microscopy-energy dispersive X-ray (STEM-EDX) line scans confirms that the elements are distributed uniformly in all the examined nanoparticles (Figure 7a–c). Shown in Figure 7d, the

dx.doi.org/10.1021/ja308674b | J. Am. Chem. Soc. 2012, 134, 18453–18459

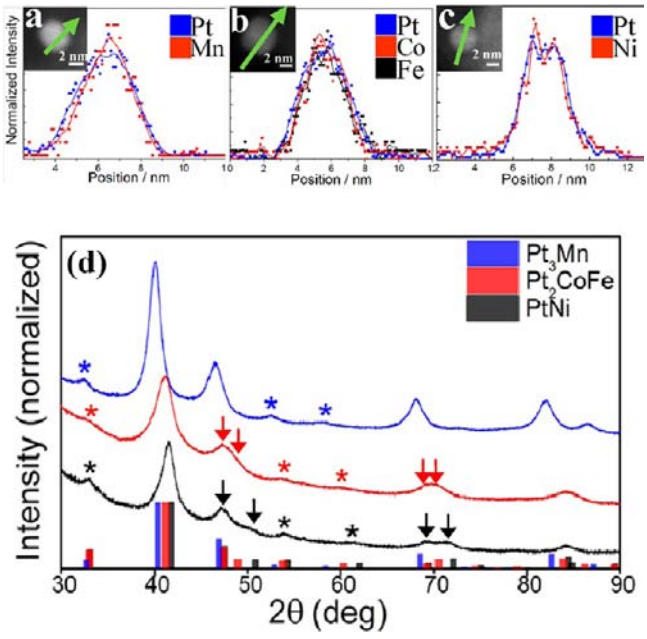

Figure 7. STEM-EDX line scans of (a) Pt_3Mn, (b) Pt_2FeCo, and (c) PtNi nanoparticles show that the elements are distributed uniformly in the particles. The best-fit lines are extrapolated by averaging adjacent points. The insets show the HAADF-STEM images of the nanoparticles scanned. (d) XRD spectra of carbon supported Pt_3Mn (blue), Pt_2CoFe (red), and PtNi (black) synthesized by thermal annealing of their Np-KCl assemblies. The lines on the bottom indicate the XRD peak positions of the corresponding intermetallic phase of the three particles (PDF card 04-002-1438 for Pt_3Mn, 01-077-7477 for Pt_2CoFe, and 03-065-2797 for PtNi). The peak positions for the ordered intermetallic phase are marked with *, and peak positions for *fct* distortions of the Pt −M 1:1 intermetallic phase are marked with arrows.

XRD pattern of Pt_3Mn nanoparticles showed a similar Pt_3M pattern as Pt_3Fe. The weak superlattice peaks at (110), (210), and (211) showed that the desired intermetallic structures were achieved. An average domain size of Pt_3Mn of 5.0 nm was calculated from the line widths of the XRD patterns. XRD of bimetallic PtNi and trimetallic Pt_2CoFe after annealing at 600 °C showed the tetragonal PtM structure. The formation of the intermetallic structure resulted in a tetragonal (*fct*) distortion of the disordered face-centered cubic PtM structure. The tetragonal distortion induces extra diffraction peaks; obvious peak splitting at around 46° for (200) and (002) as well as 70° for (220) and (202), are marked by arrows in Figure 7d. In addition to the *fct* distortion, the weak intermetallic peaks due to ordering (marked by *) of the PtNi and Pt_2CoFe nanoparticles also suggest the formation of the ordered structure observed in the bulk. Using the Scherrer equation, average crystal domain sizes of 3.4 and 4.3 nm were calculated for PtNi and Pt_2CoNi, respectively. The detailed synthesis and annealing procedures for these three nanoparticles are given in the Supporting Information. Here, we are using these preliminary results to show that this method is applicable to bi- and trimetallic intermetallic nanoparticles with different electronegativity and structure types. A more detailed report on the synthesis of a variety of such systems will be reported in future publications.

CONCLUSION

This contribution demonstrates a novel strategy to synthesize nanoparticles in desired phase (crystalline order) and of a desired size without using organic surfactants, which may decompose on the particle surface, often irreversibly during thermal annealing. In this method, KCl serves as a matrix that traps the nanoparticles to avoid particle agglomeration and to control the coalescence of nanoparticles during thermal annealing. As an example, Pt_3Fe-ordered alloy catalysts with average particle sizes around 4 and 2.5 nm were synthesized by this method. We found that the nanoparticles can be released from the salt in an ethylene glycol−water solvent mixture and would then uniformly bind to a carbon black support with little agglomeration. Electrochemical studies of the 4-nm Pt_3Fe catalyst showed an improved ORR efficiency when compared to those of pure Pt. The origin of the improved ORR properties is not the focus of this report; however, on the basis of our previous results, the ordered intermetallic phase of the core in the resulting core−shell particles appears to play an important role in the improvement. More importantly, this Np-KCl strategy is not limited to the synthesis of Pt_3Fe nanoparticles. Our preliminary results on the synthesis of Pt_3Mn PtNi and Pt_2CoFe intermetallic nanoparticles showed that this method is applicable to a wider variety of transition metals and ordered structure types.

ASSOCIATED CONTENT

Supporting Information

Some further discussion and more figures and tables. This material is available free of charge via the Internet at http://pubs.acs.org.

AUTHOR INFORMATION

Corresponding Author

fjd3@cornell.edu

Notes

The authors declare no competing financial interest.

ACKNOWLEDGMENTS

This work was supported by the Basic Energy Sciences Division of the Department of Energy through Grant DE-FG02-87ER45298. D.W. was supported by DOE through the Energy Materials Center at Cornell, an EFRC supported by Grant DE-SC0001086. We thank Mick Thomas for help with the EDX data acquisition and analysis and John Grazul for help with the TEM data acquisition and analysis. The author would also wish to thank Brian M. Leonard (University of Wyoming, United States) for the early discussions on this work. The EDX and TEM facility are managed and maintained by the Cornell Center for Materials Research (CCMR), an NSF supported MRSEC through Grant DMR-1120296. Y.Y. acknowledges the fellowship support from the American Chemical Society (ACS) Division of Analytical Chemistry (ACS) sponsored by Eastman Chemical Company.

REFERENCES

(1) Sun, Y. G.; Wiley, B.; Li, Z. Y.; Xia, Y. N. *J. Am. Chem. Soc.* **2004**, *126*, 9399.
(2) Alivisatos, A. P. *Science* **1996**, *271*, 933.
(3) Collier, C. P.; Saykally, R. J.; Shiang, J. J.; Henrichs, S. E.; Heath, J. R. *Science* **1997**, *277*, 1978.

(4) Sun, S. H.; Murray, C. B.; Weller, D.; Folks, L.; Moser, A. *Science* **2000**, *287*, 1989.
(5) Kim, J. M.; Rong, C. B.; Liu, J. P.; Sun, S. H. *Adv. Mater.* **2009**, *21*, 906.
(6) Stamenkovic, V.; Mun, B. S.; Mayrhofer, K. J. J.; Ross, P. N.; Markovic, N. M.; Rossmeisl, J.; Greeley, J.; Norskov, J. K. *Angew. Chem., Int. Ed.* **2006**, *45*, 2897.
(7) Stamenkovic, V. R.; Mun, B. S.; Mayrhofer, K. J. J.; Ross, P. N.; Markovic, N. M. *J. Am. Chem. Soc.* **2006**, *128*, 8813.
(8) Strasser, P.; Koh, S.; Anniyev, T.; Greeley, J.; More, K.; Yu, C. F.; Liu, Z. C.; Kaya, S.; Nordlund, D.; Ogasawara, H.; Toney, M. F.; Nilsson, A. *Nature Chem* **2010**, *2*, 454.
(9) Casado-Rivera, E.; Volpe, D. J.; Alden, L.; Lind, C.; Downie, C.; Vazquez-Alvarez, T.; Angelo, A. C. D.; DiSalvo, F. J.; Abruna, H. D. *J. Am. Chem. Soc.* **2004**, *126*, 4043.
(10) Greeley, J.; Stephens, I. E. L.; Bondarenko, A. S.; Johansson, T. P.; Hansen, H. A.; Jaramillo, T. F.; Rossmeisl, J.; Chorkendorff, I.; Norskov, J. K. *Nature Chem* **2009**, *1*, 552.
(11) Forgie, R.; Bugosh, G.; Neyerlin, K. C.; Liu, Z. C.; Strasser, P. *Electrochem. Solid State* **2010**, *13*, D36.
(12) Arico, A. S.; Bruce, P.; Scrosati, B.; Tarascon, J. M.; Van Schalkwijk, W. *Nat. Mater.* **2005**, *4*, 366.
(13) Armand, M.; Tarascon, J. M. *Nature* **2008**, *451*, 652.
(14) Lu, Y. C.; Xu, Z. C.; Gasteiger, H. A.; Chen, S.; Hamad-Schifferli, K.; Shao-Horn, Y. *J. Am. Chem. Soc.* **2010**, *132*, 12170.
(15) Kim, J.; Lee, Y.; Sun, S. H. *J. Am. Chem. Soc.* **2010**, *132*, 4996.
(16) Yamamoto, S.; Morimoto, Y.; Tamada, Y.; Takahashi, Y. K.; Hono, K.; Ono, T.; Takano, M. *Chem. Mater.* **2006**, *18*, 5385.
(17) Yamamoto, S.; Morimoto, Y.; Ono, T.; Takano, M. *Appl. Phys. Lett.* **2005**, *87*, 032503−1.
(18) Tamada, Y.; Yamamoto, S.; Takano, M.; Nasu, S.; Ono, T. *Appl. Phys. Lett.* **2007**, *90*, 162509−1.
(19) Wang, D. L.; Subban, C. V.; Wang, H. S.; Rus, E.; DiSalvo, F. J.; Abruna, H. D. *J. Am. Chem. Soc.* **2010**, *132*, 10218.
(20) Bock, C.; Paquet, C.; Couillard, M.; Botton, G. A.; MacDougall, B. R. *J. Am. Chem. Soc.* **2004**, *126*, 8028.
(21) Wang, Y.; Ren, J. W.; Deng, K.; Gui, L. L.; Tang, Y. Q. *Chem. Mater.* **2000**, *12*, 1622.
(22) Bonet, F.; Guery, C.; Guyomard, D.; Urbina, R. H.; Tekaia-Elhsissen, K.; Tarascon, J. M. *Int. J. Inorg. Mater.* **1999**, *1*, 47.
(23) Bonet, F.; Delmas, V.; Grugeon, S.; Urbina, R. H.; Silvert, P. Y.; Tekaia-Elhsissen, K. *Nanostruct. Mater.* **1999**, *11*, 1277.
(24) Zhang, S.; Guo, S.; Zhu, H.; Su, D.; Sun, S. *J. Am. Chem. Soc.* **2012**, *134*, 5060.
(25) Abe, H.; Matsumoto, F.; Alden, L. R.; Warren, S. C.; Abruna, H. D.; DiSalvo, F. J. *J. Am. Chem. Soc.* **2008**, *130*, 5452.
(26) Roychowdhury, C.; Matsumoto, F.; Mutolo, P. F.; Abruna, H. D.; DiSalvo, F. J. *Chem. Mater.* **2005**, *17*, 5871.
(27) Ghosh, T.; Leonard, B. M.; Zhou, Q.; DiSalvo, F. J. *Chem. Mater.* **2010**, *22*, 2190.
(28) Wikander, K.; Ekstroem, H.; Palmqvist, A. E. C.; Lindbergh, G. *Electrochim. Acta* **2007**, *52*, 6848.
(29) Holby, E. F.; Sheng, W. C.; Shao-Horn, Y.; Morgan, D. *Energy Environ. Sci.* **2009**, *2*, 865.
(30) Leonard, B. M.; Zhou, Q.; Wu, D. M.; DiSalvo, F. J. *Chem. Mater.* **2011**, *23*, 1136.
(31) Strong, J.; Tuttle, T. R. *J. Phys. Chem.* **1973**, *77*, 533.
(32) Garrett, D. E. *Handbook of Lithium and Natural Calcium Chloride: Their Deposits, Processing, Uses and Properties*, 1st ed.; Elsevier Academic Press: Amsterdam; Boston, 2004.
(33) Warren, B. *X-ray Diffraction*; Dover Publications: Mineola, NY, 1990.
(34) Kirkland, E. J.; Loane, R. F.; Silcox, J. *Ultramicroscopy* **1987**, *23*, 77.
(35) Crewe, A. V.; Wall, J.; Langmore, J. *Science* **1970**, *168*, 1338.
(36) Yu, Y.; Xin, H. L.; Hovden, R.; Wang, D.; Rus, E. D.; Mundy, J. A.; Muller, D. A.; Abruña, H. A. *Nano Lett.* **2012**, *12*, 4417.
(37) Skoplyak, O.; Barteau, M. A.; Chen, J. G. G. *Surf. Sci.* **2008**, *602*, 3578.
(38) Skoplyak, O.; Barteau, M. A.; Chen, J. G. *ChemSusChem.* **2008**, *1*, 524.
(39) Skoplyak, O.; Menning, C. A.; Barteau, M. A.; Chen, J. G. G. *Top. Catal.* **2008**, *51*, 49.
(40) Salciccioli, M.; Yu, W. T.; Barteau, M. A.; Chen, J. G. G.; Vlachos, D. G. *J. Am. Chem. Soc.* **2011**, *133*, 7996.
(41) Wang, C.; Wang, G. F.; van der Vliet, D.; Chang, K. C.; Markovic, N. M.; Stamenkovic, V. R. *Phys. Chem. Chem. Phys.* **2010**, *12*, 6933.
(42) Wang, D.; Yu, Y.; Xin, H. L.; Hovden, R.; Ercius, P.; Mundy, J. A.; Chen, H.; Richard, J. H.; Muller, D. A.; DiSalvo, F. J.; Abruña, H. D. *Nano Lett.* **2012**, *12*, 5230 DOI: 10.1021/nl302404g.
(43) Strasser, P.; Koh, S.; Anniyev, T.; Greeley, J.; More, K.; Yu, C.; Liu, Z.; Kaya, S.; Nordlund, D.; Ogasawara, H.; Toney, M. F.; Nilsson, A. *Nature Chem* **2010**, *2*, 454.
(44) Oezaslan, M.; Heggen, M.; Strasser, P. *J. Am. Chem. Soc.* **2011**, *134*, 514.
(45) Koh, S.; Strasser, P. *J. Am. Chem. Soc.* **2007**, *129*, 12624.
(46) Yu, Y.; Xin, H. L.; Hovden, R.; Wang, D.; Rus, E. D.; Mundy, J. A.; Muller, D. A.; Abruña, H. D. *Nano Lett.* **2012**, *12*, 4417.
(47) Stamenković, V.; Schmidt, T. J.; Ross, P. N.; Marković, N. M. *J. Phys. Chem. B* **2002**, *106*, 11970.
(48) Carlton, C. E.; Chen, S.; Ferreira, P. J.; Allard, L. F.; Shao-Horn, Y. *J. Phys. Chem. Lett.* **2012**, *3*, 161.
(49) Mani, P.; Srivastava, R.; Strasser, P. *J. Power Sources* **2011**, *196*, 666.
(50) Zhang, J.; Yang, H.; Fang, J.; Zou, S. *Nano Lett.* **2010**, *10*, 638.
(51) Stamenkovic, V. R.; Fowler, B.; Mun, B. S.; Wang, G. F.; Ross, P. N.; Lucas, C. A.; Markovic, N. M. *Science* **2007**, *315*, 493.
(52) Wang, C.; Chi, M.; Wang, G.; van der Vliet, D.; Li, D.; More, K.; Wang, H.-H.; Schlueter, J. A.; Markovic, N. M.; Stamenkovic, V. R. *Adv. Funct. Mater.* **2011**, *21*, 147.